nature communications

Article

https://doi.org/10.1038/s41467-025-56960-1

Adaptative two-phase thermal circulation system for complex-shaped electronic device cooling

Received: 27 June 2024

Accepted: 5 February 2025

Published online: 17 February 2025

Check for updates

Wenjun Xu[1,3], Jiarong Cui[1,3], Yao Ma[1], Zhanpeng Hu[1], Yuyang Qi[1], Xinying Li[2], Yuchen Zhong[1], Tao Luo[1], Xuyang Chu[1], Linjing Wu[1], Weisong Ling[1] ✉ & Wei Zhou[1] ✉

Thermal management using a vapor-liquid two-phase circulation system is challenging in compact and complex-shaped electronic devices. In this study, we design and fabricate a heat pipe that can adapt to various shapes, regardless of space constraints. The heat pipe is capable of bending or twisting in three dimensions, making it suitable for electronic devices of arbitrary shapes. It effectively transfers heat from in-plane chips to out-of-plane spaces through flexible circulation pathways. This two-phase heat cycle system achieves an ultra-high thermal conductivity of up to 11,363 W/m·K. The flexible and adaptive design strategy enables efficient heat transfer in complex and compact environments.

The tech industry has consistently evolved towards miniaturization, with chip circuit fabrication becoming more refined and electronic device designs increasingly compact[1–3]. Conversely, the heat flux density of electronic components is rapidly increasing[4], which significantly impacting device performance[5,6]. Research shows that the lifespan of an electronic device is directly linked to its operating temperature, with every 10 °C increase potentially doubling the failure rate[7,8]. Therefore, thermal management is a crucial aspect of electronic design[9,10]. To address this issue, various technologies, such as forced air cooling and microchannel cooling, have been developed as effective heat dissipation methods.

Unfortunately, the compact size, high integration, and non-standard shapes of most emerging electronic devices[11] significantly limit direct application of many thermal management components due to space constraints. Passive thermal management technologies utilize the inherent high thermal conductivity of materials to spread heat concentrated at high heat flux density points over a larger surface area. With their small spatial requirements, high thermal conductivity, and low application costs, they have become a general solution for dissipating hot spots in compact electronic devices[12,13]. Flexible thermal film is a technological approach with high design freedom[14,15]. It can adapt flexibly to the complex surfaces of electronic devices[16,17] and offers a wide range of conformable curvatures and adjustable cooling areas[18,19], demonstrating high level of design freedom. However, single-phase solid-state conductive materials, such as graphene films or graphene paper, exhibit significant attenuation over long-distance heat transfer, limiting their effective transmission range in high heat flux density applications.

Phase-change heat transfer systems, such as micro heat pipes and vapor chambers, utilize the phase change of the working fluid to transfer heat, achieving extremely high thermal conductivity[20,21]. This is another major approach in passive thermal management. To ensure the stable operation of the phase change cycle within the heat pipe, it is necessary to maintain a high vacuum inside the system. This imposes stringent requirements on the sealing properties of the micro heat pipe. Traditional heat pipe fabrication processes typically employ welding or flattening techniques for shaping, but these methods make it difficult to construct complex three-dimensional phase-change pathways, thus limiting the design freedom of heat pipe configurations. This results in the majority of two-phase circulation systems maintaining simple 1D or 2D configuration[22,23]. Although these systems are widely applied in devices with standard shapes such as smartphones and laptops[24,25], thermal management in electronics with more complex shapes, like Augmented Reality (AR) and Virtual Reality (VR)

[1]Pen-Tung Sah Institute of Micro-Nano Science and Technology, Xiamen University, Xiamen, China. [2]State Key Laboratory of Ultra-precision Machining Technology, Department of Industrial and Systems Engineering, The Hong Kong Polytechnic University, Kowloon, Hong Kong SAR, China. [3]These authors contributed equally: Wenjun Xu, Jiarong Cui. ✉e-mail: weisongling@xmu.edu.cn; weizhou@xmu.edu.cn

headsets or cameras, is still largely confined to the plane of the chips[26] (Fig. 1a), leaving a vast untapped space available for heat distribution.

Flexible heat pipes provide a solution for transferring heat out-of-plane. Some studies use corrugated tubes as the heat pipe casing, allowing for normal and radial bending, while demonstrating good thermal conductivity[27]. However, the tubular design limits integration into most electronic devices, imposing constraints on design freedom. Alternatively, flexible composite films can be used as casings to enhance the flexibility of flat heat pipes[28,29], providing another approach for extending two-phase heat cycle pathways out-of-plane. However, this flexibility often comes at the expense of some heat transfer efficiency in structural design, and flexible deformation may cause distortion of the internal two-phase flow channels. As a result, most flexible flat heat pipes experience a reduction in heat transfer performance in three-dimensional configurations[30,31]. The deformation of most flexible flat heat pipes is typically limited to simple normal bending, significantly constraining design flexibility for more complex forms of electronic devices. Phase-change flexible filaments are another emerging technology[32]. For example, squid-inspired pulsating heat pipes[33] can achieve a thermal conductivity of up to 6750 W/m·K while offering high deformation flexibility, making them effective for spatial thermal management. However, to maximize the heat dissipation area within limited assembly spaces in electronic devices, developing phase-change cycle technologies with greater design freedom is necessary.

This work integrates customized reverse engineering with data-driven three-dimensional thermal bonding technology to design and fabricate a three-dimensional two-phase thermal circulation system that can adopt arbitrary shapes, free from assembly space constraints. This thermal circulation system is termed the adaptative heat pipe (AHP). In the AHP system, the working fluid absorbs heat under vacuum conditions, evaporating into vapor at the evaporator, which then travels along a three-dimensional vapor path, conforming to the electronic device to the condenser. At the condenser, the vapor condenses which then returns to the evaporator through the three-dimensional capillary path of the wick, establishing a continuous, two-phase, three-dimensional thermal circulation. (Fig. 1c).

The AHP possesses four degrees of design freedom: normal bending, radial bending, twisting, and lateral adjustment (Fig. 1d). It can establish stable three-dimensional phase-change pathways for electronic devices with any curved surfaces and complex configurations (as Supplementary Movie 1), achieving a maximum thermal conductivity of 11363 W/m·K. The AHP technology was compared with various passive thermal management technologies in terms of thermal conductivity and design freedom. The AHP maintains the ultra-high thermal conductivity advantage of the gas-liquid phase-change cycle while offering design freedom in any shape (Fig. 1e). Therefore, in practical applications, the AHP thermal circulation system can be considered a material with ultra-high thermal conductivity, featuring integrated structure-function characteristics. In this work, the AHP serves not only as a thermal management component integrated into the electronic device but also as internal support, or even as part of the device's shell or other structural components. The special three-dimensional shape alters the characteristics of the vapor-liquid two-phase cycle, endowing the phase change cycling system with multi-functional and intelligent features, providing application patterns for the next generation of phase change heat transfer systems.

Results

The freeform construction method of AHP

To address the challenges of producing complex-shaped adaptative heat pipes, we present a rapid and cost-effective solution for customized fabrication. Instead of directly printing heat pipes using selective laser melting (SLM) technology, this work utilizes digital light processing (DLP) 3D printing technology for the indirect fabrication of complex-shaped AHP. The designed AHP structure, shown in Fig. 1c consists of two components: the heat pipe casing and the self-supporting wick. The casing is composed of two layers of aluminum-plastic film, with the composition detailed in Supplementary Fig. 2. Due to the thermoplastic properties of the inner polypropylene layer, applying pressure at a specific temperature allows for thermal bonding of the aluminum-plastic film casing. The internal structure includes a self-supporting wick, created from three-dimensionally structured multi-layer copper mesh. The capillary force of the wick is enhanced by chemically deposited hydrophilic nanosheets (as detailed in Supplementary Fig. 3). The self-supporting wick and the aluminum-plastic film casing collaborate to form a vapor-liquid co-planar two-phase circulation structure. The wick functions as the liquid pathway, while an independent vapor pathway is created between the wick and the casing. By using the cross-section as the design unit for AHP enables the topology of two-phase circulation along any path of the three-dimensional coordinate system, which forms the foundation for the freeform design of AHP.

During the design process, a customized 3D configuration of the AHP must be determined based on the complex shape of the target electronic device. Inspired by reverse engineering techniques in architecture, we have developed a reverse design strategy for customized AHP, as shown in Fig. 1f. Taking Mixed Reality (MR) headset as an example, the design process starts by converting the target model into spatial point cloud data (Fig. 1fI). Trajectories are planned along the edges and areas of abrupt curvature of the target, and critical point coordinates on these trajectories are extracted (Fig. 1fII–III). As the aluminum-plastic film shell needs to be transformed from an initial 2D plane into a 3D curved surface, the 2D shape of the aluminum-plastic film must be defined according to the 3D surface to prevent sealing defects. Triangular meshes are generated between points on adjacent trajectories to form the 3D surface (Fig. 1fVI). Then, using a topological equivalence mapping algorithm, the corresponding 2D plane shape of the 3D surface is generated (Fig. 1fV). The detailed description of the algorithm can be found in the method section.

In the fabrication process, a major challenge is the thermal bonding of the Al/plastic film casing with a 3D curved surface, which directly impacts the sealing capability of the two-phase circulation system. Two key factors are identified in the thermal bonding process: temperature and pressure. In this work, the fastening force of bolts provides three-dimensional normal pressure, while Joule heat generated by flexible carbon fabric as an internal heat source. Customized resin molds are created based on the extracted trajectory points by DLP photopolymerization 3D printing technology (Supplementary Fig. 4a). Carbon fabric is used as a flexible heater and is assembled with the heat pipe components in a customized 3D-printed resin mold. The thermal edge sealing of the complex-shaped casing is achieved by the combined effects of three-dimensional pressure and internal heat (Supplementary Fig. 4c). The detailed description of the fabrication method is provided in the method section and Supplementary Movie 2. The AHP customized for MR headset efficiently performs two-phase thermal cycling under complex three-dimensional configurations (Fig. 1fVI). Its spatial thermal management performance under the effect of a point heat source is illustrated by thermal imaging, as shown in Fig. 1fVII. Due to the characteristics of two-phase cycling heat transfer, a relatively uniform temperature distribution is maintained over the entire annular curved surface.

We selected typical 3D complex electronic devices such as cameras, unmanned aerial vehicles, and lamps as design targets. The trajectory point clouds of their casings were extracted, and AHPs with customized shapes were fabricated. The customized AHP conforms to the freeform surface of target electronic devices, establishing a three-dimensional vapor-liquid two-phase circulation path and performing out-plane 3D thermal management in these devices, as shown in Fig. 1g.

https://doi.org/10.1038/s41467-025-56960-1

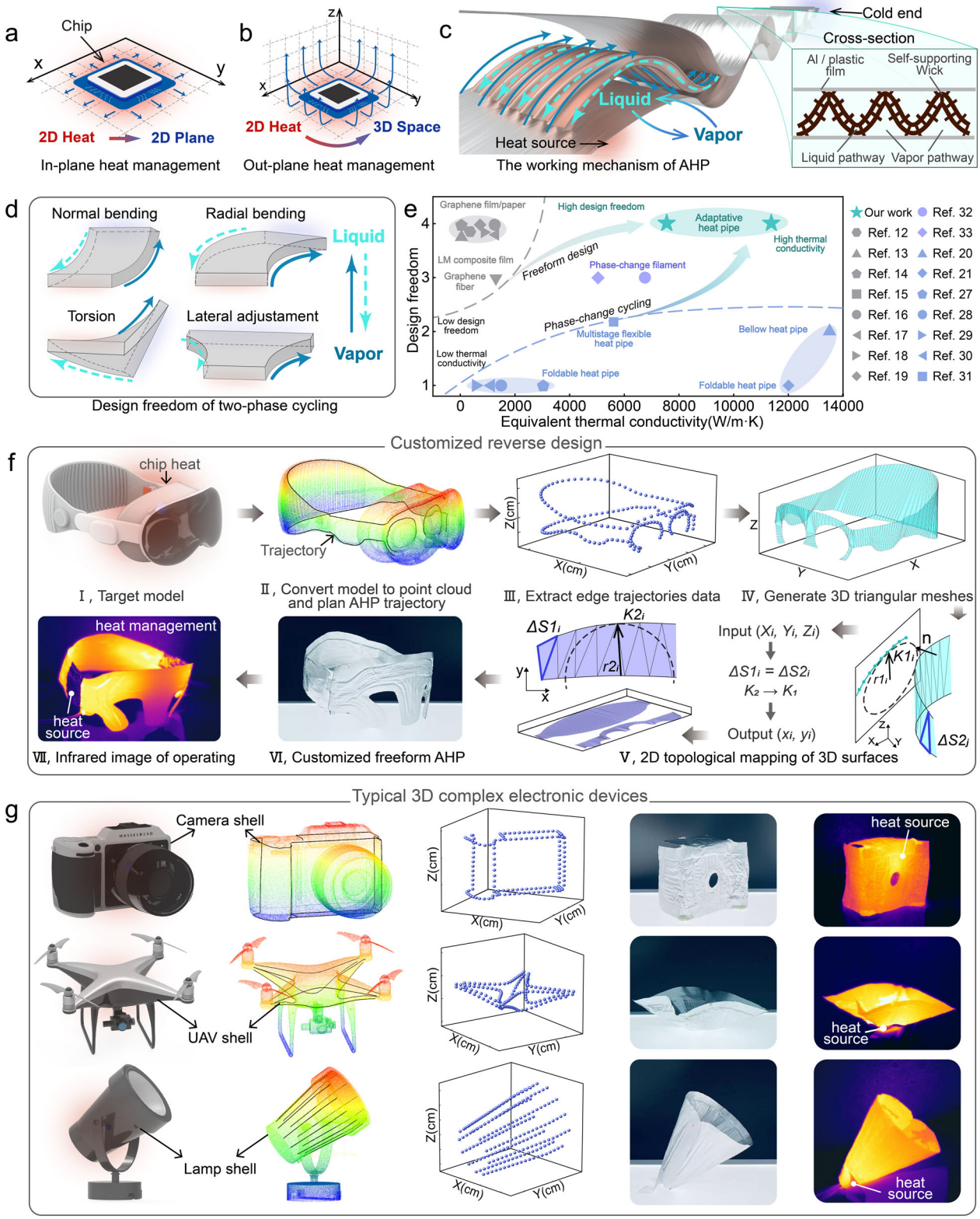

Fig. 1 | Conceptual illustration and customized design strategy for the adaptative heat pipe (AHP) in complex 3D electronic devices. a In-plane thermal management of traditional phase change system in electronic device. **b** Out-plane thermal management of 3D two-phase circulation by AHP. **c** Working mechanism and the structure of AHP, consisting of a self-supporting wick and aluminum-plastic film casing to form a vapor-liquid co-planar two-phase circulation structure. **d** Design freedom of two-phase heat cycle pathways inside the AHP. **e** Comparison of design freedom and thermal conductivity among AHP, single-phase heat conduction, and flexible two-phase heat cycle technologies. **f** Reverse design of AHP (Illustrated with the mixed reality headset example). **g** Custom conformal AHP for typical complex 3D electronic devices.

https://doi.org/10.1038/s41467-025-56960-1

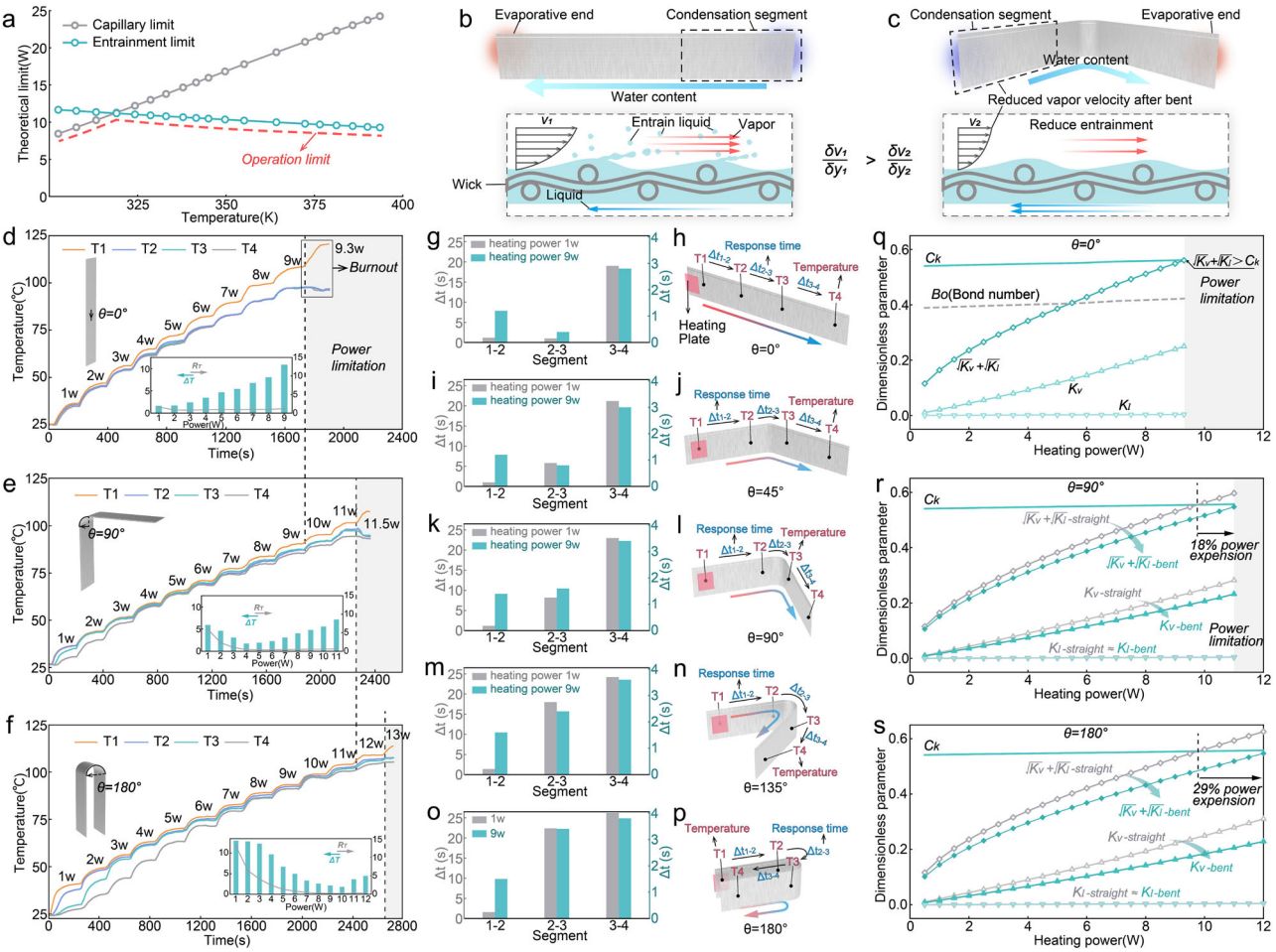

Fig. 2 | Mitigation effects of 3D segment on two-phase counterflow entrainment. a Theoretical operating limits of adaptative heat pipe (AHP). **b** Entrainment effects in 2D two-phase counterflow. **c** Schematic of mitigated two-phase counterflow entrainment in 3D AHP. **d** Operating performance of AHP without 3D segment. **e** Operating performance of AHP with 90° local 3D segment. **f** Operating performance of AHP with 180° local 3D segment. Thermal response time and testing illustration for normal bending angles of (**g**, **h**) 0°, (**i**, **j**) 45°, (**k**, **l**) 90°, (**m**, **n**) 135°, and (**o**, **p**) 180° local 3D segments. **q** Theoretical prediction of entrainment limit for AHP without 3D sections. **r** Modified theoretical prediction of the entrainment limit for AHP with a 90° local 3D segment. **s** Modified theoretical prediction of the entrainment limit for AHP with a 180° local 3D segment.

The influence of 3D shape on the entrainment effect in two-phase counterflow

The operating limit of a heat pipe is the maximum heat capacity it can transfer. When the heat source exceeds this limit, it disrupts the two-phase cycle within the heat pipe, leading to operating failure. Based on heat pipe theory, there are five critical limits for heat pipes[34]. To investigate the impact of the 3D segment on heat pipe performance, we initially conducted theoretical calculations on the two-phase thermal cycle limit under the basic structural parameters of AHP, as shown in Fig. 2a (The theoretical derivation process can be found in Supplementary Note 1). Calculations show that within the typical operating temperature range of micro heat pipes using water as the working fluid, the AHP is primarily limited by the capillary limit and the entrainment limit. The capillary limit occurs when the pressure drop during the two-phase cycle exceeds the capillary force provided by the wick[35], failing to satisfy Eq. (1). As a result, the working fluid cannot circulate back quickly enough, causing the evaporator to dry out. The entrainment limit occurs at the vapor-liquid interface, where excessively high relative speeds of vapor and liquid counterflow, lead to the vapor entraining the working liquid back towards the condenser[36,37], as illustrated in Fig. 2b.

$$\Delta P_{cp} \geq \Delta P_v + \Delta P_l + \Delta P_g \quad (1)$$

To characterize the 3D shape of AHP parametrically, the normal bending state of the heat pipe is used as the fundamental 3D configuration, as illustrated in Fig. 2c. When the AHP is straight, i.e., with a bending angle of 0°, its operating performance is as shown in Fig. 2d. Thermocouples are placed at both the hot and cold ends of the AHP, and two additional thermocouples are positioned equidistantly at the middle section. The straight AHP shows the smallest temperature difference between the cold and hot ends ($\Delta T1-4 = T1 - T4$) at 1 W. As the heating power increases, $\Delta T1-4$ gradually increases, indicating that the straight AHP operates more efficient two-phase circulation at low power input. When the heating power reaches 9.3 W, the temperature at the hot end (T_1) rises rapidly, whereas the other temperature points (T_2, T_3, T_4) fail to follow. This indicates that the evaporator of the AHP cannot absorb the increased power, thus reaching its operating limit. By introducing a 3D segment with a 90° bending angle in the AHP (Fig. 2e), the minimum $\Delta T1-4$ is observed at 4 W, and the heat transfer limit extends to 11.5 W, an increase of 23.7%. When the normal bending angle is increased to 180° (Fig. 2f), the minimum $\Delta T1-4$ occurs at 10 W, and the operating limit is further increased to 13 W (an increase of 44.4%). Supplementary Fig. 6a–c further illustrated the heat transfer performance of AHP with normal bending angles of 45° and 135°. The results indicate that the operating limit of the AHP occurs within the power range of the entrainment limit.

Increasing the normal bending angle improves the AHP's operating limit. This suggests that the 3D configuration of the heat pipe potentially mitigates the occurrence of the entrainment limit.

By combining theoretical formulas, we further investigated the mechanism of the mitigation effect of 3D configurations on the entrainment limitation. The entrainment limit for the vapor-liquid interface can be theoretically calculated using flooding correlations in a counterflow vapor-liquid system. The criteria for entrainment instabilities can be determined using Eq. (2)[37].

$$(k_v)^{\frac{1}{2}} + (k_l)^{\frac{1}{2}} = \sqrt{3.2}\,\tanh(0.5Bo^{\frac{1}{4}}) \equiv C_k \tag{2}$$

The Bond number (Bo) is a dimensionless parameter characterizing the interface fluid properties (Eq. (3)), primarily determined by the surface tension σ of working fluid and characteristics parameter D for the interface. k_v and k_l respectively represent the dimensionless momentum fluxes of the vapor and liquid phase (Detailed calculation formulas are provided in Supplementary Note 2).

$$Bo = D[g(\rho_l + \rho_v)/\sigma]^{\frac{1}{2}} \tag{3}$$

We theoretically calculated the entrainment limit at different input powers, as shown in Fig. 2q. The results reveal that as power increases, the most noticeably changing variable is the dimensionless momentum flux of the vapor k_v, suggesting that the drastic variation in vapor velocity as power changes is crucial in influencing the entrainment effect. Due to the high sealing requirement, directly measuring vapor flow velocity inside the heat pipes at micro-scales is challenging. Therefore, we indirectly assessed vapor velocity across different 3D configurations by measuring the thermal response time and revising entrainment limit criteria for 3D configurations. The normal bending angles tested were 0°(Fig. 2g, h), 45°(Fig. 2i, j), 90°(Fig. 2k, l), 135°(Fig. 2m, n), and 180°(Fig. 2o, p), respectively. Four thermocouples were placed at the same positions on the AHP for different 3D configurations, and the thermal response time intervals between $T1$ and the other three points were measured upon contact of the heating plate at the evaporator, with input powers of 1 W and 9 W. $\Delta t1-2$, $\Delta t2-3$, and $\Delta t3-4$ represents the thermal response time of the vapor flow before the 3D segment, through the 3D segment, and from the 3D segment to the cold end, respectively. The results show that as the bending angle increases, there is negligible change in $\Delta t1-2$, while $\Delta t2-3$ significantly increases, and $\Delta t3-4$ shows a modest increase. The extended thermal response time due to the 3D sections primarily results from changes in vapor flow, while liquid flow is more influenced by the wick's capillary structure. As illustrated in Supplementary Figs. 7–12, the introduction of curved sections primarily affects the vapor flow pressure drop, and changes in liquid pressure drop are negligible. In addition to momentum exchange, the vapor-liquid interface of the wick undergoes evaporation and condensation of the working fluid, resulting in complex flow conditions[38,39]. With an increasing bending angle, the flow behavior at the interface becomes more complex as high-speed vapor passes through the bending section. Consequently, the thermal response time for vapor to pass through the 3D segment is greatly extended, while the straight segment after the 3D segment shows a minor reduction in thermal flow velocity due to reduced momentum. By modifying the momentum flux based on the increments of $\Delta t3-4$ at different bending angles, as illustrated in Fig. 2r, s, we found that the predictions for the entrainment limit closely align with the increases in the power limit. Since the condensation mainly occurs at the condenser of the heat pipe, leading to a higher concentration of working fluid at this segment, entrainment is more likely to occur. Therefore, the construction of the 3D segment able to mitigate entrainment occurrence in the condenser segment.

Additionally, we constructed local 3D segments at different locations along the two-phase cycle path of the AHP and evaluated heat transfer performance, as shown in Supplementary Fig. 13a. Results showed that constructing a local 3D segment at the condenser reduces the maximum power of the AHP by 1 W compared to other locations. This reduction could be attributed to significant interactions at the vapor-liquid interface within the 3D pathway, which adversely affects the liquid return at the condenser, where the liquid concentration is higher. A detailed description can be seen in Supplementary Fig. 13.

The robustness of AHP to spatial state changes

Wearable and mobile electronic devices frequently change spatial state based on user demands, which often prevents their cooling components from operating in the most advantageous state. In two-phase thermal circulation systems, spatial state changes affect the gravitational pressure drop, represented by ΔPg in Eq. (1). To ensure the stable operation of the AHP, it is essential to minimize gravitational pressure drop changes across various spatial states. We theoretically calculated the capillary driving force, vapor pressure drop, and liquid pressure drop of the AHP at different heating powers and identified the maximum allowable gravitational pressure drop, as shown in Supplementary Fig. 14. The results show that as power increases, the theoretically permissible range of gravitational pressure drop gradually decreases. By discretizing the AHP and defining the spatial state change parameters α and β, and calculating the weighted average of the gravitational pressure drops across the discrete segments, we derived the formula for the 3D gravitational pressure drop of the AHP in various spatial states, as Eq. (4). The complete derivation is provided in Supplementary Note 3.

$$P_g = \sum_{k=1}^{n} \frac{l_k}{L} \rho g \,\sin(\theta_k(\alpha,\beta)) \tag{4}$$

We selected three different heat pipe configurations: a straight flat heat pipe (2D), a fully deformed 3D AHP (full 3D), and an AHP with 3D deformation in the middle section while the remaining section remains flat (partial 3D). All three heat pipes maintain a complete two-phase heat cycle pathway, effectively eliminating the impact caused by structural collapse in flexible heat pipes under deformation. The primary difference lies in the gravitational pressure drop of the liquid working fluid across different spatial orientations. Using the gravitational pressure drop formula for AHP, we evaluated the theoretical changes in gravitational pressure drops for 2D, partial 3D, and full 3D configurations of AHP across six spatial states, as shown in Fig. 3b. The results indicate that the maximum change in gravitational pressure drop for the 2D straight heat pipe across different spatial states is 2560 Pa. For AHP with partial 3D and full 3D configurations, the maximum changes are 870 Pa and 960 Pa, respectively, equating to 34% and 37.5% of that for the straight 2D heat pipe. A smaller change in gravitational pressure drop indicates that spatial state variations have less impact on the heat pipe's operational performance, enhancing the robustness of electronic devices against spatial changes in practical applications.

The operating performance of AHP was evaluated across different configurations. After stabilizing at a heating power of 8 W, the 2D heat pipe and the 3D AHP underwent sequential spatial state changes, with temperatures at the hot and cold ends recorded. The results indicate that with changes in spatial state, the straight 2D heat pipe exhibits significant temperature fluctuations between the hot and cold ends, which increase the temperature gradient, severely disrupting the vapor-liquid two-phase cycle (Fig. 3c). In contrast, both the partial 3D (Supplementary Fig. 15) and full 3D (Fig. 3d) configurations of AHP maintain relatively stable temperatures at the hot and cold ends, resulting in minimal changes in the temperature difference. Theoretical calculations indicate that the

https://doi.org/10.1038/s41467-025-56960-1

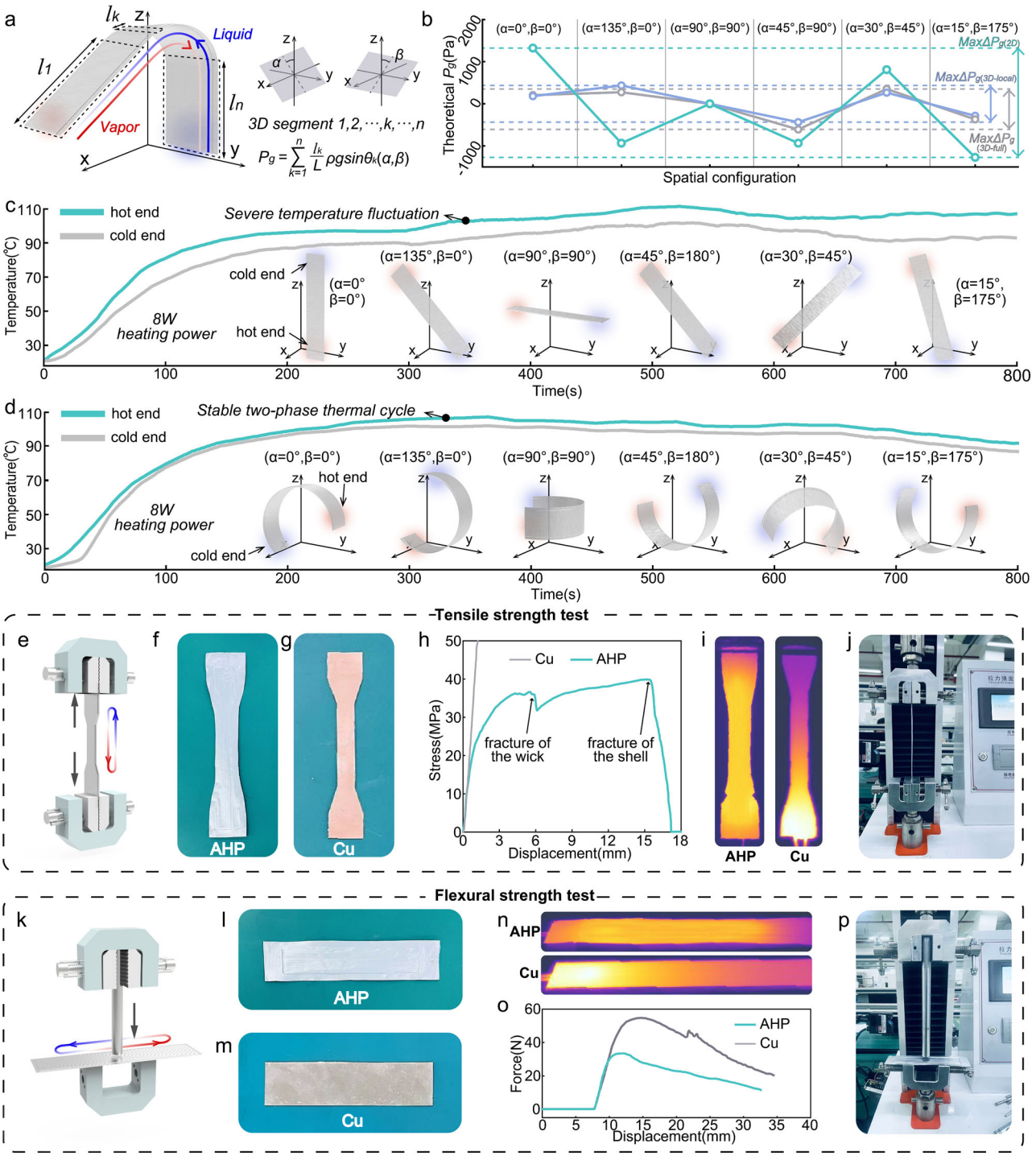

Fig. 3 | Spatial robustness and mechanical strength testing of the adaptative heat pipe (AHP). a Discrete weighted calculation of gravitational pressure drop in AHP. **b** Theoretical values of gravitational pressure drop in different spatial states. **c** Heat transfer performance of the straight 2D heat pipe across different spatial states. **d** Heat transfer performance of the AHP with full 3D segment across different spatial states. **e** Schematic diagram of the AHP tensile test. **f** An AHP in the shape of tensile specimens. **g** A copper heat dissipation sheet in the shape of tensile specimens. **h** Heat transfer performance of the tensile-shaped AHP and copper sheet under 4 W heating power. **i** Tensile stress-strain curve of the AHP. **j** Tensile test of the AHP. **k** Schematic diagram of the AHP flexural test. **l** An AHP in the shape of flexural specimens. **m** A copper heat dissipation sheet in the shape of flexural specimens. **n** Heat transfer performance of the flexural-shaped AHP and copper sheet under 4 W heating power. **o** Flexural stress-strain curve of the AHP. **n** Flexural test of the AHP.

permissible gravitational pressure drop for the straight 2D heat pipe across six spatial states is 1281 Pa, with a maximum resistance to gravitational pressure drop of 1203.2 Pa, which is close to the permissible limit. This results in considerable variations in capillary backflow resistance for the straight 2D heat pipe across different spatial states, indicating weaker robustness to spatial changes. The 3D configured AHP, with smaller variations in gravitational pressure drop, has maximum gravitational pressure drops of 435.7 Pa and 609.2 Pa across different spatial states, significantly below the allowable limits. This indicates good spatial robustness, making it suitable for the spatial state changes required by compact electronic devices.

Mechanical strength of AHP

With its freeform design characteristics, the AHP can integrate into the mechanical assembly of electronic devices in various forms, similar to two-dimensional thermal materials, while maintaining efficient phase-change heat transfer performance. It exhibits integrated structural and functional application characteristics. To demonstrate the structural support properties of the AHP as a casing or support component for electronic devices, we conducted tensile and flexural tests and compared the results with those of commercial copper heat dissipation plates. Given the thin-plate structure of the AHP, we designed a dumbbell-shaped tensile specimen (tensile section width of 10 mm) and conducted tensile tests on both the AHP and copper plates (Fig. 3e–g). The tensile strength of the AHP ranges between 30 and 40 MPa (Fig. 3h), similar to that of rigid plastics like epoxy resin (20.67–40 MPa)[40–42]. Although the tensile strength of AHP shows a significant difference compared to copper (>200 MPa), it is sufficient to meet the mechanical requirements of most mobile and wearable device enclosures. Moreover, the internal two-phase cycle enables the AHP to exhibit extremely high thermal conductivity as a device-level application material, as shown in Fig. 3i.

The AHP, composed of a composite structure with an aluminum-plastic film casing and a copper wire mesh wick, undergoes multiple mechanical stages during the tensile test. In the initial tension stage, the aluminum-plastic film casing and copper wire mesh wick transition from elastic deformation to plastic deformation (Supplementary Fig. 16aI–II). When the tensile stress reaches 36.18 MPa, a slight decrease in tensile stress is observed. The images indicate that at this point, while the heat pipe casing remains intact, the AHP elongates slightly, primarily due to the fracture of the internal wick. Subsequently, the aluminum-plastic film continues to stretch (Supplementary Fig. 16aIII), and the tensile stress-displacement curve shows characteristics of plastic deformation, resulting in complete fracture when the tensile stress reaches 40.01 MPa (Supplementary Fig. 16aIV).

Additionally, due to the thin-plate structure of the AHP, a flexural performance test was conducted (Fig. 3k). The AHP and copper plate specimens were prepared as rectangles with a length of 150 mm and a width of 30 mm (Fig. 3l–m). Under a heating power of 4 W, the AHP displayed a more uniform temperature gradient, while the copper plate exhibited uneven temperature distribution (Fig. 3n), with significant heat accumulation at the hot end. The resulting pressure-displacement curve is shown in Fig. 3o. Compared to the tensile performance, the difference in flexural performance between the two thin-plate materials is smaller: the maximum pressure for the copper plate is 54.7 N, while for the AHP it is 37.68 N, approximately 68.9% of the copper plate's value.

Out-plane 3D thermal management of customized AHP in a VR headset

The assembly of thermal management components is often a key point of contention between thermal engineers and structural designers in electronic device design. The AHP design utilizes the available space after other components are installed, free from the spatial constraints, to achieve out-plane 3D thermal management. Moreover, AHP possesses integrated structural-functional characteristics. Beyond its two-phase thermal circulation function, it can also serve as a casing or support component, further enhancing the compactness of electronic devices. As representative products of compact and complex-shaped devices, virtual reality (VR) headsets are widely adopted in both industrial and home settings[43,44]. Research indicates that the face is the one of the most heat-sensitive parts of human body[45,46]. VR headset panels typically feature an enclosed design, leading to significant heat accumulation during operation[47]. However, compact and complex device configurations hinder the effective integration of thermal management components[48].

Here, we designed a customized AHP specifically tailored to the special construction of VR headsets, deviating from the conventional design of regular-shaped cooling components. The customized AHP functions not only as a thermal management element but also as part of the head-mounted component, allowing the heat from the simulated chip to be directly transferred through the AHP for natural convection with the external air and maximizing the cooling area within limited assembly space. A schematic of the VR device is shown in Fig. 4a. To ensure alignment with the VR device's structural characteristics, the AHP contacts the simulated chip at the center of the panel, distributing the heat along three separate paths. This heat is then transferred outside through gaps between the face pad and the control panel, extending along three head straps to form a closed-loop structure. The installation of the customized AHP in the VR headset, as illustrated in Fig. 4b, demonstrates that the AHP configuration conforms to the structural characteristics of the VR headset.

In commercial applications, flat microheat pipes are used as cooling components in VR devices due to their two-phase thermal cycling characteristics. For instance, the Quest Pro VR headset by Meta Inc. integrates flat heat pipes within the panel for chip cooling[26]. Additionally, graphene thermal films, an emerging electronic cooling strategy, are used in some electronic products due to their high flexibility and thermal conductivity[49–51]. To assess the 3D two-phase thermal management efficiency of AHP, it was compared with commercial flat heat pipes and graphene films in a VR headset (as Supplementary Movie 3). Detailed structural and assembly information is provided in Supplementary Figs. 17–20. With a 4 W heating power applied to the simulated chip, thermal management performance is shown in Fig. 4c–e. Due to the heat transfer characteristics of two-phase cycling, 2D flat heat pipes exhibit uniform temperature distribution. However, constrained by the 2D form, they can only manage heat within the plane of the panel, limiting the cooling area and resulting in the hot end temperature exceeding 100 °C (Fig. 4c). As a flexible cooling material, graphene film can manage heat in three dimensions according to device shape, but it is limited by the properties of single-phase thermal conduction. The graphene film exhibits a significant temperature gradient, with hot end reaching 84.7 °C (Fig. 4d). A customized AHP combines the phase-change cooling capabilities of 2D flat heat pipes with the design freedom of graphene film, achieving comprehensive 3D two-phase circulation cooling for VR devices. As shown in Fig. 4e, AHP maintains excellent temperature uniformity, reducing the temperature to 47.8 °C under the same power input.

We compared the chip temperature under different cooling conditions and input powers, as shown in Fig. 4f. Without cooling measures, the simulated chip heat diffuses throughout the panel via direct contact, reaching 100 °C at 2 W and exceeding 120 °C at 3 W. When a 2D micro heat pipe is installed on the panel, the heating power can be stabilized at 3 W, with the hot end temperature reaching 83 °C. At 4 W, the temperature at the hot end exceeds 100 °C. Installing graphene film along the head strap significantly increases the heat dissipation area and enhances cooling performance compared to the 2D heat pipe, allowing the heating power to increase further to 5 W. With the integration of AHP, a significant reduction in temperature is observed. At the input power of 3 W, the average temperature of the simulated chip decreased by 48.59% (from 85°C to 43.7 °C) and 38.62% (from 71.2 °C to 43.7 °C) compared to the 2D heat pipe and graphene film, respectively. Additionally, combined with the 3D configuration's mitigation effects of two-phase counterflow entrainment, the customized AHP shows a pronounced advantage in the improved heat transfer limit. Taking 100 °C as the limit, the simulated chip temperature exceeds 100 °C at 4 W with the 2D heat pipe and at 6 W with graphene film. With AHP cooling, however, the simulated chip can be increased to 19 W, an increment of 4.75 and 3.17 times compared to the 2D heat pipe and graphene film, respectively.

The AHP demonstrates structural-functional integration. Specifically designed for head-mounting components, the customized AHP not only performs two-phase thermal circulation but also

https://doi.org/10.1038/s41467-025-56960-1

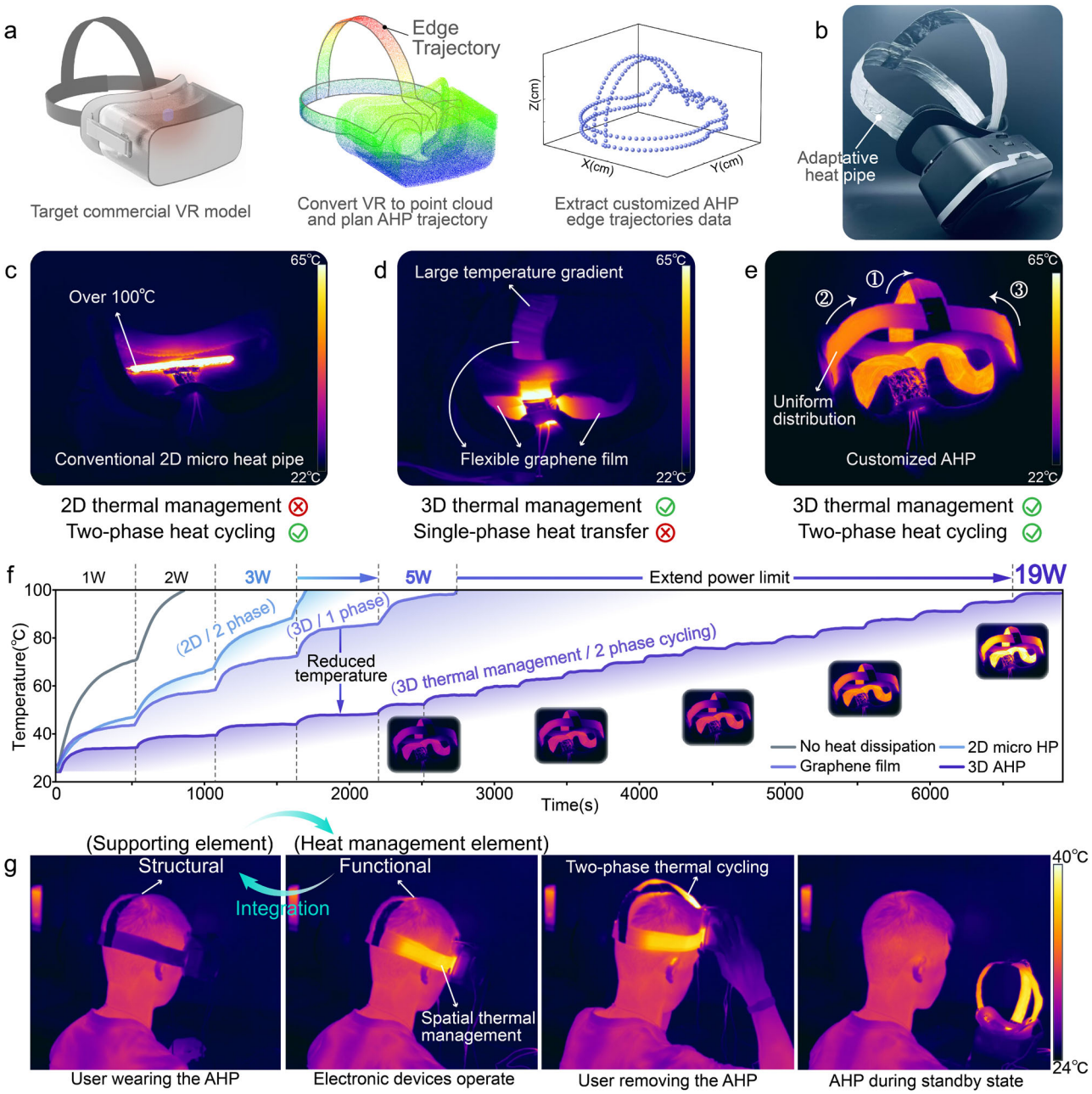

Fig. 4 | Customized adaptative heat pipe (AHP) for VR headset. a Reverse design of the AHP for the VR headset, extracting the head-mount component to create a customized AHP that provides both cooling capability and mounting functionality. **b** VR headset after co-integration of the AHP. **c** Infrared thermal imaging results of the commercial flat heat pipe under a heating power of 4 W. **d** Infrared thermal imaging of the commercial flexible graphene film under simulated chip heating power of 4 W. **e** Infrared thermal imaging of the customized AHP under simulated chip heating power of 4 W. **f** Comparison of the temperatures at the hot end for the customized AHP, conventional flat micro heat pipe, and commercial flexible graphene film across different power settings. **g** User testing of the structural-functional integrated AHP.

provides structural support for the user's head. As shown in Fig. 4g, user testing was conducted with a simulated chip heating power of 6 W, during which the highest temperature maintained by the customized AHP was 43 °C. Under the same power settings, temperatures for commercial cooling strategies exceed 100 °C, posing burn risks to users. Detailed information on the user testing is provided in Supplementary Movie 4.

Stretchable two-phase circulation system

In electronic devices, thermal management components like heat pipes will operate two-phase circulation under extreme environments[52]. Intense vibrations experienced during spacecraft launches or while driving automobiles can significantly impact electronic devices[53,54]. In addition, potential heat transfer requirements between cross-axis planes of aerospace robotic arms (Supplementary Fig. 21) pose a severe challenge to traditional heat pipe technology. Special 3D structural design can impart exceptional mechanical properties and advanced functions to the device[55]. By utilizing the freeform design characteristics of AHP, we have developed a stretchable AHP with a spiral three-dimensional shape, targeting the spring components in shock absorbers (Fig. 5a). This design allows the heat pipe to extend over a long-range, functioning similarly to a spring. It adapts to dynamic spatial relationships between heat transfer planes, ensuring stable heat exchange.

https://doi.org/10.1038/s41467-025-56960-1

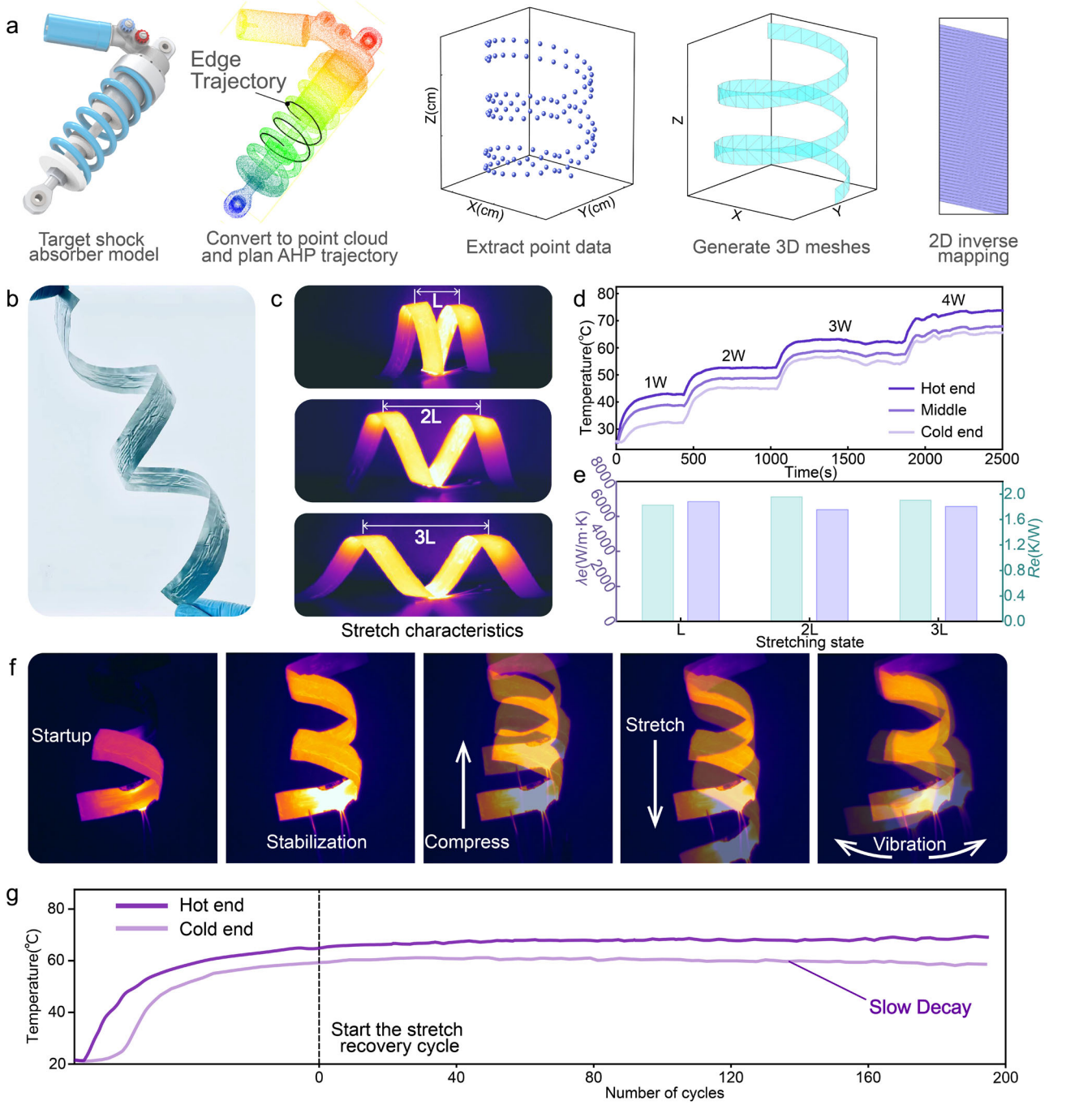

Fig. 5 | Development of stretchable vapor-liquid phase-change circulation system. a Extraction of spring element curves from the shock absorber enables the designed adaptative heat pipe (AHP) to offer not only heat exchange capabilities but also damping and stretchability. **b** A stretchable AHP. **c** Characteristics of the stretchable AHP (L represents the minimum pitch of the stretchable heat pipe). **d** Dynamic temperature distribution curves of the stretchable heat pipe under different heating powers. **e** Heat transfer performance of the stretchable heat pipe under different stretching conditions. **f** Operation of the stretchable AHP under simulated extreme conditions, including compression, stretching, mild vibration, and intense vibration. **g** Cycle test of compression and stretching for the stretchable AHP.

The developed stretchable AHP and its dynamic operating state are shown in Fig. 5b, with its two-phase circulation during dynamic stretching illustrated in Fig. 5c. The axial length can be compressed from 2L to L and extended to 3 L, achieving a threefold extension range. Heat transfer performance tests were conducted on the stretchable heat pipe with a pitch of 2 L under different heating powers. As shown in Fig. 5d, temperatures were measured at three locations: the hot end (15 mm from the edge), the cold end (20 mm from the edge), and the middle section, with temperature changes recorded as heating power increased from 1 W to 4 W. Results indicate that as heating power increased from 1 W to 4 W, the temperature difference between the hot and cold ends decreased from 11 °C to 9 °C, with a thermal resistance of 2.34 K/W and a thermal conductivity of 5335 W/m·K. In a helical configuration, the AHP has minimal curvature changes without smooth transition sections. This results in less effective curvature coordination between the membrane layers on both sides of the heat pipe during fabrication, causing some compression of the internal wick and affecting the stretchable AHP's heat transfer efficiency.

However, in the constructed 3D helical two-phase heat cycle pathway, the macroscopic deformation from mechanical stretching has minimal impact on the stretchable heat pipe. As shown in Fig. 5e, thermal conductivity of the stretchable heat pipe was measured under various stretching states. When the pitch of the stretchable heat pipe is L, 2 L, or 3 L, its heat transfer performance shows minimal variation, with thermal resistance fluctuating within ±0.15 K/W.

Heat transfer operation between different planes of the AHP was simulated, as shown in Fig. 5f. After thermal stabilization, the AHP underwent compression, stretching, mild vibration, and intense vibration (complete process available in Supplementary Movie 5). Thermal imaging revealed no severe performance loss in the AHP. After thermal stabilization, a test of 200 compression and extension cycles was conducted (Fig. 5g). Fluctuations were observed in the temperature at the heat pipe's hot end. These fluctuations may be attributed to changes in vapor pathways during compression and extension and to slight compression of the two-phase structure during stretching. Additionally, the hot end temperature remained relatively stable within 65.5 °C to 68.5 °C, while a gradual decrease in cold end temperature was observed. This suggests that while the stretching cycles affected the heat pipe performance, they did not cause edge leakage or significant blockage in the two-phase cycle. Instead, the fluctuations likely result from deformation of the two-phase structure due to repeated stretching and compression.

Magnetically-controlled two-phase circulation heat exchange robot

The fourth industrial revolution, marked by advancements in information technology and artificial intelligence, has ushered in the era of intelligence, making device smartification an inevitable path for future development[56]. In thermal management, a key challenge is the cooling random hot spots, specifically dynamic heat dissipation when point heat source coordinates change over time. Leveraging the freeform design property of the adaptative heat pipe, we introduce the concept of vapor-liquid two-phase circulation heat exchange robots, developing intelligent application modes for conventional phase change systems.

The AHP was designed as an enclosed cube (Fig. 6a), with the entire cube serving as a unified vapor-liquid two-phase circulation path (Fig. 6b). Its two-dimensional mapping form is shown in Fig. 6c, with the two-phase cycling path marked in the diagram. As shown in Fig. 6d–e, the heat transfer performance of the heat exchange robot achieves a maximum thermal conductivity of 4699 W/m·K with the heat source on surface 3. The thermal conductivity between surface 3 and surface 1 is 3720 W/m·K, and between surface 3 and surface 6 is 3524 W/m·K. After fabricating the cubic AHP, magnets with different polarizations were embedded inside each of the six faces, forming the AHP heat exchange robot. Leveraging its cubic 3D form, the AHP heat exchange robot can be maneuvered by flipping through the magnetic field at the base, allowing it to approach coordinates of randomly generated hot spots (Fig. 6f). When the AHP heat exchange robot covers a hot spot, heat is quickly conducted away through the robot's two-phase circulation walls, preventing further heat accumulation (Fig. 6g). To illustrate the design concept of the AHP heat exchange robot, we simulated its operation under random heat sources, as shown in Fig. 6h (for a detailed view, see Supplementary Movie 6). When a random hot spot emerges within the plane (Fig. 6hI), the AHP robot quickly flips and moves closer to the hot spot (Fig. 6hII–III). By contacting the hot spot with its bottom wall, the robot uses the fast startup and efficient heat transfer of its two-phase circulation walls to rapidly disperse heat throughout the entire shell of the robot, expanding the originally localized air convection area to all six faces of the cube (Fig. 6hIV). After the first hot spot dissipates, a second one forms (Fig. 6hV). The AHP heat exchange robot continues to flip, contact, and dissipate the hot spot (Fig. 6hVI–VII) and then moves to the next hot spot (Fig. 6hVIII).

Discussion

In summary, the AHP developed in this work leverages reverse engineering and data-driven three-dimensional thermal bonding technology, functioning as a phase-change circulation system with unprecedented shape design freedom. The three-dimensional two-phase thermal cycling path is customized to the configuration and thermal requirements of target electronic devices, facilitating direct heat exchange between the chip and the external environment, offering a solution to thermal management challenges in small, compact, and complex-shaped electronic devices.

The three-dimensional pathway improves the heat transfer limit of the vapor-liquid phase-change system and potentially mitigates entrainment effects at the vapor-liquid interface in counterflow. Theoretical calculations based on flooding correlations reveal vapor flow rate as a key factor under varying input powers. Adjusting the correlation equations with velocity attenuation aligns calculated power increases closely with experimental measurements. Moreover, compared to 2D phase-change systems, 3D two-phase systems exhibit enhanced robustness to spatial state changes under high power conditions. Under spatial state changes, the maximum theoretical gravitational pressure drop for the 3D-configured AHP reduced to 34% of that in the 2D configuration. This diminished influence of gravity on two-phase circulation meets the spatial state change requirements of wearable and mobile electronic devices.

This study developed a customized AHP tailored for VR headset structures. Compared to commercial flat 2D heat pipes and graphene films, the customized AHP reduced the simulated chip temperature by 48.59% (41.3 °C) and 38.62% (27.5 °C), respectively, at the same input power of 3 W. It also increased the power limit by 4.75 times (from 4 W to 19 W) and 3.17 times (from 6 W to 19 W), respectively. The three-dimensional configuration endows the AHP with integrated structural-functional characteristics, enabling it to serve as both a thermal management component and a head-mounted structure, providing structural support. The AHP's spiral and cubic designs impart features such as stretchability and dynamic heat dissipation, paving the way for multifunctional and intelligent development of two-phase thermal circulation systems.

Methods

Fabrication of freeform AHP

In the fabrication process, DLP 3D printing technology is first used to create molds for shaping the copper wire mesh and pre-encapsulating the AHP (Supplementary Fig. 4a). The mold for the copper mesh is designed to serve as the self-supporting structure for the wick, while the heat pipe sealing mold is designed with space reserved exclusively for the edges of the AHP, ensuring contact only at the these points.

As shown in Supplementary Fig. 4b, the mold shapes the copper mesh into a three-dimensional form by assembling multiple layers of flat copper mesh within it. Thanks to the high flexibility and ductility of the copper mesh, upon releasing the bolts, the multi-layer copper mesh retains the customized shape of the AHP at the macro level and forms a self-supporting structure of the wick at the micro level. The formed multi-layer copper mesh then undergoes sintering and chemical deposition processes to form stable capillary pores and enhance hydrophilicity.

The aluminum-plastic film, wick, flexible carbon fabric, and mold are assembled together and secured with bolts to apply pressure. To generate heat for the thermal bonding process, apply voltage to both sides of the carbon fabric for Joule heating. This step completes the thermal bonding of the aluminum-plastic film casing, forming a complex three-dimensional shape (Supplementary Fig. 4c). After releasing

https://doi.org/10.1038/s41467-025-56960-1

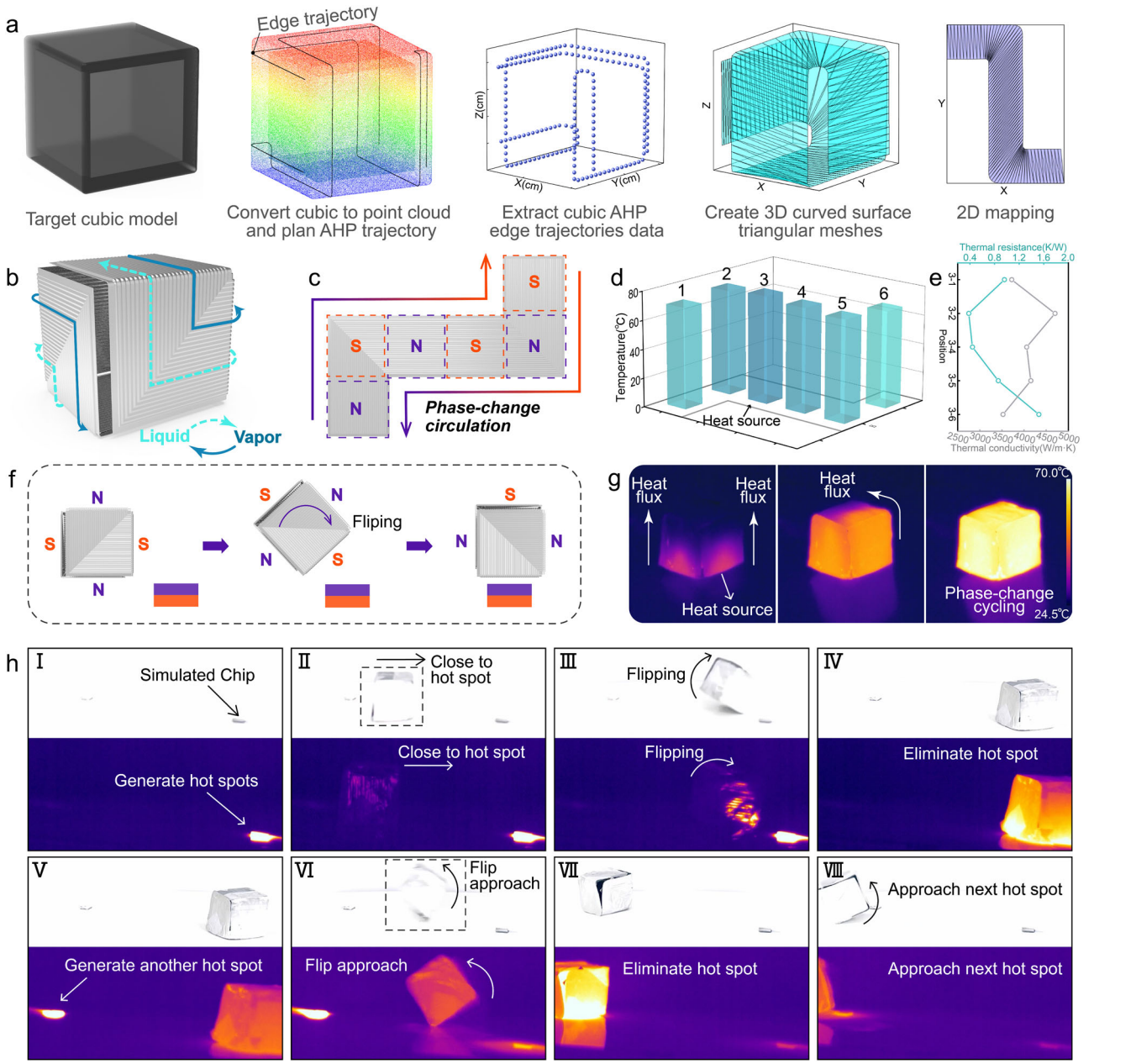

Fig. 6 | Dynamic cooling of two-phase circulation heat exchange robot system. **a** Extraction of external curves of the cubic model to plan the two-phase circulation path of the adaptative heat pipe (AHP) and construct a fully enclosed cubic AHP. **b** Structural schematic of a cubic AHP. **c** Schematic of magnetic pole arrangement for heat exchange robot. **d** Temperature distribution at the center points of the six faces under a bottom point heat source. **e** Thermal resistance and thermal conductivity at a heating power of 5 W. **f** Magnetic actuation flipping method for the AHP heat exchange robot. **g** Heat transfer process demonstrated by the cubic AHP when positioned above a hot spot. **h** The AHP heat exchange robot performing dynamic heat dissipation in response to random hot spots (The upper and lower sections of the diagram respectively represent the workflow under an optical camera and an infrared thermal imaging camera).

the bolts, a pre-encapsulated AHP (three sides sealed, one side open) is obtained.

Next, venting treatment is performed through a charging port on the pre-encapsulated AHP, followed by vacuuming and filling with working fluid (deionized water). The final side is then sealed to complete the fabrication of a customized AHP with two-phase thermal cycling capabilities. Detailed information about the fabrication process is provided in Supplementary Fig. 5 and Supplementary Movie 2, offering a more intuitive understanding of the fabrication method.

Materials

Aluminum-plastic film (D-EL40H(3)) as heat pipe casing was purchased from Dai Nippon Printing Co., Japan. Copper wire mesh (200 mesh copper) used as wick was purchased from Anping County Bolin Metal Wire Mesh Co., China. The carbon fabric (WOS1009, CeTech, USA) after cutting, was utilized as a flexible heater. Chemicals including sodium persulfate ($Na_2S_2O_8$), sodium hydroxide (NaOH), deionized water, and ethanol were purchased from Shanghai Aladdin Biochemical Technology Co.

3D printing of shaping and pre-encapsulating molds

A customized configuration of the three-dimensional resin mold is created using Computer-Aided Design (CAD) software and exported in STL format. This STL file is then imported into Voxeldance Tango slicing software to add support structures and slice the model. The sliced file is loaded into a Digital Light Processing (DLP) 3D printing machine

(Reflect2, DONZY, China). The printing parameters are set as follows: light source intensity at 5 mW/cm², exposure time at 2.5 s, and layer thickness at 50μm. Begin the printing process. After printing, the mold is removed and immersed in an ultrasonic cleaner (SK5210LHC, KUDOS, China) filled with 95% alcohol, with the cleaning parameters set to 53 kHz and 150 W for 60 s. After ultrasonic cleaning, the mold is dried in a 60 °C oven (DZF−6020, Shanghai Jinghong, China).

Topological equivalence mapping algorithm

The implementation of the 2D topological mapping algorithm for the AHP 3D triangular sheet is conducted using commercial software MATLAB. Trajectory planning of the three-dimensional point cloud is performed in CloudCompare software to obtain point coordinates along the trajectory, forming 3D triangular meshes between points on two closely adjacent trajectories. This forms the basis for mapping the surface from 3D triangular meshes to a corresponding 2D plane, guiding the planar shape design of the aluminum-plastic film casing. The specific process for implementing the topological mapping algorithm is described as follows:

Step 1: Identified the central triangle mesh within the triangulated surface model to serve as the base triangle for mapping.

Step 2: Map the base triangle onto the plane while preserving its spatial characteristics unchanged. Mark the corresponding vertices, edges, and triangle as unmapped.

Step 3: Identified the adjacent 3D triangular mesh, $\Delta 1_i$, that currently processing. Among the triangular meshes that are not yet marked as unmapped, select one that shares an edge with a triangle already marked as unmapped to be the current triangle under processing.

Step 4: Confirm the position of the undetermined vertex of the currently processed triangle in the 2D plane. Calculate the normal vector passing through this point in the 3D surface, and determine the normal plane $\overrightarrow{n}$ corresponding to this normal vector $\overrightarrow{P_n}$. Select a vertex adjacent to the vertex currently being processed, and determine the projection of this adjacent vertex on the normal plane $\overrightarrow{P_n}$ of the 3D surface. Then, calculate the curvature $K1_i$ at the processed vertex. In the 2D plane, ensure that the curvature $K2_i$ of the undetermined point is the same as $K1_i$. This approach can allow determine the direction between the undetermined point and its adjacent point. To determine the 2D position of the currently processed point, ensure that the area $S2_i$ of the triangle in the 2D plane matches the area $S1_i$ of its counterpart in 3D space.

Step 5: Mark the currently processed point and the triangular surface as unmapped, record the number of unmapped triangles, and repeat steps 3 and 4.

Hydrophilic treatment of wick

The capillary force of the wick significantly influences the performance of heat pipes[57]. To efficiently fabricate wicks with intricate three-dimensional shapes, flexible copper wire mesh is used. The capillary pores are created by sintering multi-layered copper wire mesh, and hydrophilic capillary structures on the copper mesh surface are formed via chemical deposition[31,58], with detailed procedures depicted in Supplementary Fig. 3. The process begins with precise cutting of copper mesh using a pulsed laser. The layered copper mesh is then assembled within a mold to achieve complex three-dimensional forms. To enhance the bonding strength between layers and stabilize the capillary pores, the shaped multi-layer copper wire mesh undergoes a sintering process. Subsequently, the samples are cleaned with ultrasonic cleaning and treated chemically, with the reaction formula presented in Eqs. (5)–(7)[59,60]. After hydrophilic treatment, the surface of wick features CuO micro/nano hydrophilic structures (Supplementary Figs. 23–24), forming the liquid pathway for two-phase circulation of AHP. The contrast in hydrophilicity of the wick before and after the hydrophilic treatment is demonstrated in Supplementary Fig. 25.

$$Cu + 2NaOH + Na_2S_2O_8 \rightarrow Cu(OH)_2 + Na_2SO_4 \quad (5)$$

$$Cu(OH)_2 + 2OH^- \rightarrow [Cu(OH)_4]^{2-} \quad (6)$$

$$[Cu(OH)_4]^{2-} \rightarrow CuO \downarrow + H_2O + 2OH^- \quad (7)$$

Characterization

The morphology of hydrophilic wick in Supplementary Fig. 23 was captured by Scanning Electron Microscopy (SUPRA55 SAPPHIRE, ZEISS, German), as well as the energy dispersive X-ray spectrometer (EDS) in Supplementary Fig. 24. The structure of wick was observed by optical microscope (AO-HK830, Aosvi Co. Ltd, China). The thermal imaging of the AHP during startup and stable operation were recorded by an infrared thermal imaging camera (FLIR T440, FLIR Systems Company, USA).

Experimental setup

The testing setup for evaluating the performance of the AHP includes a DC power supply (WPS3010B, Shenzhen WANPTEK Electronic Technology Co., China), a data acquisition system (34901 A, KEYSIGHT, USA), Type K thermocouples (Omega, USA), and a heating plate (10 cm × 10 cm). The heating plate is mounted 10 mm from the edge on the hot end of the AHP. Thermal conductive silicone grease (6.5 W/m·K) is applied between the heating plate and AHP to minimize contact thermal resistance. Two thermocouples are positioned at each end of the AHP: one at the hot end, 10 mm from the heat pipe's edge, and the other at the cold end, 15 mm from the edge. Additional thermocouples are evenly placed in the middle, conforming to the customized shape of the AHP, to assess thermal distribution throughout the device. The temperatures recorded by the thermocouples are captured by the data acquisition system and transmitted to a computer. The temperatures measured at the hot and cold ends are used to compute the heat pipe's thermal resistance[31,61] and thermal conductivity[21,62], with the calculation formulas detailed in Supplementary Note 4. A parametric study on the heat transfer performance of the AHP structure was conducted, with variations in parameters such as thickness, length, and width. Test results and analysis are provided in Supplementary Figs. 26–27.

Numerical methodology

To streamline the computational model and focus on the impact of the heat pipe's geometry on the two-phase cycle, the simulation employs a design featuring distinct vapor and liquid fields, encapsulated by a metal film layer that serves as the heat pipe's shell, as depicted in Supplementary Fig. 28. Cuboids with an area of 10 × 10 mm² and a thickness of 0.3 mm are used as both the heating plate and condenser. Their centers are located 15 mm from the heat pipe's ends, positioned near the wall on the wick side (Supplementary Fig. 28b, c). To maintain a uniform total length for the two-phase circulation across all models, the central line length of the various 3D heat pipes is kept consistent with that of a straight heat pipe.

The operation of the two-phase cycle in the heat pipe is simulated using COMSOL Multiphysics 6.2. This simulation employs the Laminar Flow module to analyze vapor flow within the vapor chamber, the Brinkman Equations module for describing liquid flow within the wick, and the Porous Media Heat Transfer module for addressing heat transfer across different sections of the heat pipe. Non-isothermal flow multiphysics coupling integrates the Laminar Flow and Brinkman Equations modules.

The effect of gravity may vary and become complex under different deformation conditions. To eliminate the influence of gravity, the gravity option is disabled in both the Laminar Flow and Brinkman Equations modules. The vapor chamber boundary is set to the vapor pressure of water. To maintain equal water mass flux between the vapor chamber and wick field, velocity boundary conditions are set at their interface.

$$\mathbf{u}_2 = \frac{\mathbf{u}_1 \cdot \rho_2}{\rho_1} \tag{8}$$

Where $\boldsymbol{u}$ represents the fluid velocity vector, and ρ denotes density. The subscript 1 refers to the vapor chamber domain, and subscript 2 refers to the wick domain. Heat exchange during the evaporation-condensation process is simulated by adding a boundary heat source at the interface between the vapor chamber and the wick.

$$Q_b = \mathbf{u}_n \cdot h_{fg} \cdot \rho \tag{9}$$

Where $\boldsymbol{u_n}$ represents the normal vector of velocity u, and h_{fg} is the latent heat of vaporization of water. Simulations are conducted on heat pipes of four different shapes: straight, normal bending, radial bending, and twisting, as shown in Supplementary Fig. 28d–g. In the results, probes were placed 10 mm from the cold and hot end boundaries in both the vapor chamber and the wick to calculate the pressure drop for both the gas and liquid phases. Simulations are conducted at different angles (Supplementary Figs. 7–9) and different radius (Supplementary Figs. 10–12).

A validity test for the numerical simulation of the heat pipe is conducted following methods from reported studies[63,64]. Using the modeling setting and simulation condition provided in the referenced report[65], a numerical simulation is performed on a straight heat pipe with multiple heat sources at low-temperature operation, as depicted in Supplementary Fig. 29. Four evaporators are positioned at specific locations on one end of the straight heat pipe, with a condenser is placed at a defined coordinate on the other end (Supplementary Fig. 29a). Different power inputs are applied to each of the four evaporators, and the temperatures along the heat pipe wall are measured and compared. Since explicit cooling conditions for the condenser are not specified in the literature, various parameters are adjusted for comparison, as shown in Supplementary Fig. 29b–e.

Data availability

All data generated in this study are provided in the article, Supplementary Information and Source Data file. Source data are provided with this paper.

References

1. Van Erp, R., Soleimanzadeh, R., Nela, L., Kampitsis, G. & Matioli, E. Co-designing electronics with microfluidics for more sustainable cooling. *Nature* **585**, 211–216 (2020).
2. Lukatskaya, M. R., Dunn, B. & Gogotsi, Y. Multidimensional materials and device architectures for future hybrid energy storage. *Nat. Commun.* **7**, 12647 (2016).
3. Yang, Z., Yang, T., Cai, W. & Cai, T. Miniaturization of optical spectrometers. *Science* **371**, eabe0722 (2021).
4. Song, H. et al. Two-dimensional materials for thermal management applications. *Joule* **2**, 442–463 (2018).
5. Wang, C. et al. A thermal management strategy for electronic devices based on moisture sorption-desorption processes. *Joule* **4**, 435–447 (2020).
6. Li, M. D. et al. Thermal management of chips by a device prototype using synergistic effects of 3D heat-conductive network and electrocaloric refrigeration. *Nat. Commun.* **13**, 5849 (2022).
7. Mithal, P. Design of experimental based evaluation of thermal performance of a flichip electronic assembly (ASME EEP Proceedings, 18 ASME, New York, 1996), pp. 109–115.
8. Unsal, O. S. et al. Impact of parameter variations on circuits and microarchitecture. *IEEE Micro* **26**, 30–39 (2006).
9. Aftab, W. et al. Phase change material-integrated latent heat storage systems for sustainable energy solutions. *Energy Environ. Sci.* **14**, 4268–4291 (2021).
10. Li, W. M., Yang, S. Y., Chen, Y. P., Li, C. & Wang, Z. K. Tesla valves and capillary structures-activated thermal regulator. *Nat. Commun.* **14**, 3996 (2023).
11. Yoo, S. W. et al. Responsive materials and mechanisms as thermal safety systems for skin-interfaced electronic devices. *Nat. Commun.* **14**, 1024 (2023).
12. Wei, X. H., Liu, L., Zhang, J. X., Shi, J. L. & Guo, Q. G. Mechanical, electrical, thermal performances and structure characteristics of flexible graphite sheets. *J. Mater. Sci.* **45**, 2449–2455 (2010).
13. Vu, M. C. et al. Scalable ultrarobust thermoconductive nonflammable bioinspired papers of graphene nanoplatelet cross-linked aramid nanofibers for thermal management and electromagnetic Shielding. *J. Mater. Chem.* **9**, 8527 (2021).
14. Bartlett, M. D. et al. High thermal conductivity in soft elastomers with elongated liquid metal inclusions. *Proc. Natl Acad. Sci. USA* **28**, 2143–2148 (2017).
15. Ren, N. et al. Shear-induced fabrication of cellulose nanofibril/liquid metal nanocomposite films for flexible electromagnetic interference shielding and thermal management. *ACS Appl. Mater. Interfaces* **16**, 17904–17917 (2024).
16. Shen, B., Zhai, W. & Zheng, W. Ultrathin flexible graphene film: an excellent thermal conducting material with efficient EMI shielding. *Adv. Funct. Mater.* **24**, 4542–4548 (2014).
17. Liang, G. et al. Phase change material filled hybrid 2D/3D graphene structure with ultra-high thermal effusivity for effective thermal managemen. *Carbon* **176**, 11–20 (2021).
18. Kong, Q. Q. et al. Hierarchical graphene–carbon fiber composite paper as a flexible lateral heat spreader. *Adv. Funct. Mater.* **24**, 4222–4228 (2014).
19. Xin, G. et al. Highly thermally conductive and mechanically strong graphene fibers. *Science* **349**, 1083–1087 (2015).
20. Jaipurkar, T., Kant, P., Khandekar, S., Bhattacharya, B. & Paralikar, S. Thermo-mechanical design and characterization of flexible heat pipes. *Appl Therm. Eng.* **126**, 1199–1208 (2017).
21. Yang, C. et al. Fabrication and performance evaluation of flexible heat pipes for potential thermal control of foldable electronics. *Appl Therm. Eng.* **96**, 445–453 (2016).
22. Gibbons, M. J., Marengo, M. & Marengo, T. A review of heat pipe technology for foldable electronic devices. *Appl. Therm. Eng.* **194**, 117087 (2021).
23. Xin, F., Ma, T. & Wang, Q. Thermal performance analysis of flat heat pipe with graded mini-grooves wick. *Appl. Energy* **228**, 2129–2139 (2018).
24. Tang, H. et al. Review of applications and developments of ultra-thin micro heat pipes for electronic cooling. *Appl. Energy* **223**, 383–400 (2018).
25. Luo, J. L., Mo, D. C., Wang, Y. Q. & Lyu, S. S. Biomimetic copper forest wick enables high thermal conductivity ultrathin heat pipe. *ACS Nano* **15**, 6614–6621 (2021).
26. Meta Platforms Tech LLC. Thermal management system for electronic device. US202318242990A (2023).
27. Lee, D. & Byon, C. Fabrication and characterization of pure-metal-based submillimeter-thick flexible flat heat pipe with innovative wick structures. *Int J. Heat. Mass Transf.* **122**, 306–314 (2018).

28. Liu, C., Li, Q. & Fan, D. Fabrication and performance evaluation of flexible flat heat pipes for the thermal control of deployable structure. *Int. J. Heat. Mass Transf.* **144**, 118661 (2019).
29. Lim, J. & Kim, J. Fabrication and experimental evaluation of a polymer-based flexible pulsating heat pipe. *Energ. Convers. Manag.* **126**, 358–364 (2018).
30. Jung, C., Lim, J. & Kim, S. J. Fabrication and evaluation of a high-performance flexible pulsating heat pipe hermetically sealed with metal. *Int J. Heat. Mass Transf.* **149**, 119180 (2020).
31. Huang, J. et al. Development of novel flexible heat pipe with multistage design inspired by structure of human spine. *Appl. Therm. Eng.* **175**, 115392 (2020).
32. Kang, Z., Jiang, S., Hong, Y. & Fan, J. Squid-like soft heat pipe for multiple heat transport. *Droplet* **1**, 182–191 (2022).
33. Kang, Z., Hong, Y., Jiang, S. & Fan, J. Composite filament with super high effective thermal conductivity. *Mater. Today Phys.* **34**, 101067 (2023).
34. Reay, D. A. Kew, P. A. Heat pipes: theory, design and applications, 5th ed (Elsevier, Oxford, U.K., 2014).
35. Ma, Y. G. et al. Experimental study on sodium screen-wick heat pipe capillary limit. *Appl. Therm. Eng.* **227**, 120397 (2023).
36. Kim, B. H. & Kim, G. P. A microscale model for thin-film evaporation in capillary wick structures. *Int. J. Heat. Mass Transf.* **38**, 1427–1442 (1995).
37. Tien, C. L. Chung, K. S. "Entrainment limits in heat pipes." Presented at the 3rd International Heat Pipe Conference (American Institute of Aeronautics and Astronautics, Palo Alto, CA, USA 1978).
38. Ranjan, R., Tien, J. Y. & Tien, S. V. Analysis of the critical weber number at the onset of liquid entrainment in capillary-driven heat pipes. *Int. J. Heat. Mass Transf.* **54**, 169–179 (2011).
39. Ranjan, R., Murthy, J. Y. & Garimella, S. V. Analysis of the wicking and thin-film evaporation characteristics of wick microstructures. *ASME. J. Heat. Transf.* **131**, 101001 (2009).
40. Tesfaw, S., Bogale, T. M. & Fatoba, O. Evaluation of tensile and flexural strength properties of virgin and recycled high-density polyethylene (HDPE) for pipe fitting application. *Mater. Today Proc.* **62**, 3103–3113 (2022).
41. Cofaru, N. F., Pascu, A., Oleksik, M. & Petruse, R. Tensile properties of 3D-printed continuous-fiber-reinforced plastics. *Mater. Plast.* **58**, 271–282 (2021).
42. Tuohedi, N. & Wang, Q. Preparation and evaluation of epoxy resin prepared from the liquefied product of cotton stalk. *Processes* **9**, 1417 (2021).
43. Li, X., Yi, W., Chi, H. L., Wang, X. & Wang, A. P. C. A critical review of virtual and augmented reality (VR/AR) applications in construction safety. *Autom. Constr.* **86**, 150–162 (2018).
44. Pot-Kolder, R. M. C. A. et al. Virtual-reality-based cognitive behavioural therapy versus waiting list control for paranoid ideation and social avoidance in patients with psychotic disorders: a single-blind randomised controlled trial. *Lancet Psychiatry* **5**, 217–226 (2018).
45. Cotter, J. D. & Taylor, N. A. S. The distribution of cutaneous sudomotor and alliesthesial thermosensitivity in mildly heat-stressed humans: an open-loop approach. *J. Physiol.* **565**, 335–345 (2005).
46. Buyan, M. P. et al. Facial warming and tinted helmet visors. *Int. J. Ind. Ergon.* **36**, 11–16 (2006).
47. Ahram, T. Z. Advances in human factors in wearable technologies and game design, pp. 180–186 (Springer International Publishing, Cham, 2019).
48. Sun, Z. D., Zhu, M. L., Shan, X. C. & Lee, C. K. Augmented tactile-perception and haptic-feedback rings as human-machine interfaces aiming for immersive interactions. *Nat. Commun.* **14**, 1024 (2023).
49. Moon, J. Y. et al. Layer-engineered large-area exfoliation of graphene. *Sci. Adv.* **6**, eabc6601 (2020).
50. Fu, Y. F. et al. Graphene related materials for thermal management. *2D Mater.* **7**, 012001 (2020).
51. Li, H. L., Xiao, S. N., Yu, H. L., Xue, Y. H. & Yang, J. H. A review of graphene-based films for heat dissipation. *N. Carbon Mater.* **36**, 897–910 (2021).
52. Wang, G. et al. Recent advances in the mechanics of 2D materials. *Int. J. Extrem. Manuf.* **5**, 032002 (2023).
53. Tang, J., Tang, D., Ren, F. & Li, H. Design and experimental study of a VCM-based whole-spacecraft vibration isolation system. *J. Aerosp. Eng.* **31**, 04018045 (2018).
54. Tang, Y. et al. Noise and vibration suppression in hybrid electric vehicles: State of the art and challenges. *Renew. Sustain. Energy Rev.* **124**, 109782 (2020).
55. Cao, Z. et al. Inversely engineered biomimetic flexible network scaffolds for soft tissue regeneration. *Sci. Adv.* **9**, adi8606 (2023).
56. Meng, Q., Huang, Y., Li, L., Wu, F. & Chen, R. Smart batteries for powering the future. *Joule* **8**, 344–373 (2024).
57. Huang, X. & Franchi, G. Design and fabrication of hybrid bi-modal wick structure for heat pipe application. *J. Porous Mater.* **15**, 635–642 (2008).
58. Tang, Y. et al. Experimental investigation of capillary force in a novel sintered copper mesh wick for ultra-thin heat pipes. *Appl. Therm. Eng.* **115**, 1020–1030 (2017).
59. Chen, X. et al. Synthesis and characterization of superhydrophobic functionalized Cu(OH)2 nanotube arrays on copper foil. *Appl. Surf. Sci.* **255**, 4015–4019 (2009).
60. Zhang, Y., Yu, X., Zhou, Q., Chen, F. & Li, K. Fabrication of superhydrophobic copper surface with ultra-low water roll angle. *Appl. Surf. Sci.* **256**, 1883–1887 (2010).
61. Min, C., Gao, X., Gao, F. & Wang, K. Thermal performance analyses of pulsating heat pipe for application in proton exchange member fuel cell. *Energy Convers. Manag.* **259**, 115566 (2022).
62. Mehrali, M. et al. Effect of nitrogen-doped graphene nanofluid on the thermal performance of the grooved copper heat pipe. *Energy Convers. Manag.* **118**, 459–473 (2016).
63. Mahdavi, M. Faghri, A. "The effects of bending on heat pipes." Presented at the ASME 2021 Heat Transfer Summer Conference (American Society of Mechanical Engineers, 2021).
64. Rice, J. & Faghri, A. Analysis of screen wick heat pipes, including capillary dry-out limitations. *J. Thermophys. Heat. Transf.* **21**, 475–486 (2007).
65. Naphon, P. & Wongwises, S. A review of flow and heat transfer characteristics in curved tubes. *Renew. Sust. Energy Rev.* **10**, 463–490 (2006).

Acknowledgements

We acknowledge the financial support from the National Natural Science Foundation of China (grants 52325507 to W.Z., U21A20136 to W.Z., 52205497 to W.S.L.), the National Natural Science Foundation of Xiamen (grants 3502Z20227027 to W.S.L.), the Fundamental Research Funds for the Central Universities (grants 20720230074 to W.S.L.). We acknowledge Mr Y.L.J. and Dr Y.Q.Y. from Goertek Technology Co., Ltd. for their technical support and advice.

Author contributions

W.X. conceived the idea. W.Z. and W.L. supervised the work. W.X., W.L., T.L., X.C., and W.Z. conceptualized the study. W.X. and Y.M. designed the solution. W.X., J.C., Z.H., and Y.Q. fabricated the samples. W.X. and J.C. carried out the characterization. W.X., Y.M., X.L., and Y.Z. performed the computational studies. W.X. prepared the original draft. W.X., L.W., W.L., and W.Z. reviewed and edited the manuscript.

Competing interests

The authors declare no competing interests.

Additional information

Supplementary information The online version contains supplementary material available at https://doi.org/10.1038/s41467-025-56960-1.

Correspondence and requests for materials should be addressed to Weisong Ling or Wei Zhou.

Peer review information *Nature Communications* thanks Zhanxiao Kang, Sreekant Narumanchi, and the other, anonymous, reviewer for their contribution to the peer review of this work. A peer review file is available.

Reprints and permissions information is available at http://www.nature.com/reprints

Publisher's note Springer Nature remains neutral with regard to jurisdictional claims in published maps and institutional affiliations.

Open Access This article is licensed under a Creative Commons Attribution-NonCommercial-NoDerivatives 4.0 International License, which permits any non-commercial use, sharing, distribution and reproduction in any medium or format, as long as you give appropriate credit to the original author(s) and the source, provide a link to the Creative Commons licence, and indicate if you modified the licensed material. You do not have permission under this licence to share adapted material derived from this article or parts of it. The images or other third party material in this article are included in the article's Creative Commons licence, unless indicated otherwise in a credit line to the material. If material is not included in the article's Creative Commons licence and your intended use is not permitted by statutory regulation or exceeds the permitted use, you will need to obtain permission directly from the copyright holder. To view a copy of this licence, visit http://creativecommons.org/licenses/by-nc-nd/4.0/.

© The Author(s) 2025